Reversible, Stable and Uniform SERS in a Y-shaped Microfluidic Chip: Chemical Imaging of Concentration Gradients

Supplementary Material (SM)

F. Chauvet

Laboratoire de Génie Chimique, Université de Toulouse, CNRS, Toulouse INP, UTIII, France

1 3D numerical simulation of heat transfer in the SERS microfluidic chip

The steady state temperature field in the SERS microfluidic chip is obtained by numerical simulation using the software Comsol. The considered geometry consists of three rectangular blocks: one for the bottom glass plate, one for the flowing liquid and one for the top glass plate (the thickness of the SERS substrate is neglected), Fig. SM 1. The symmetry plane *xz* (parallel to the flow direction and shown in blue in Fig. SM 1) is used to reduce computation time. The energy conservation equation is solved in each of the three domains.

*Corresponding author: fabien.chauvet@univ-tlse3.fr; +33 5 61 55 74 68; ORCID 0000-0002-3102-0368

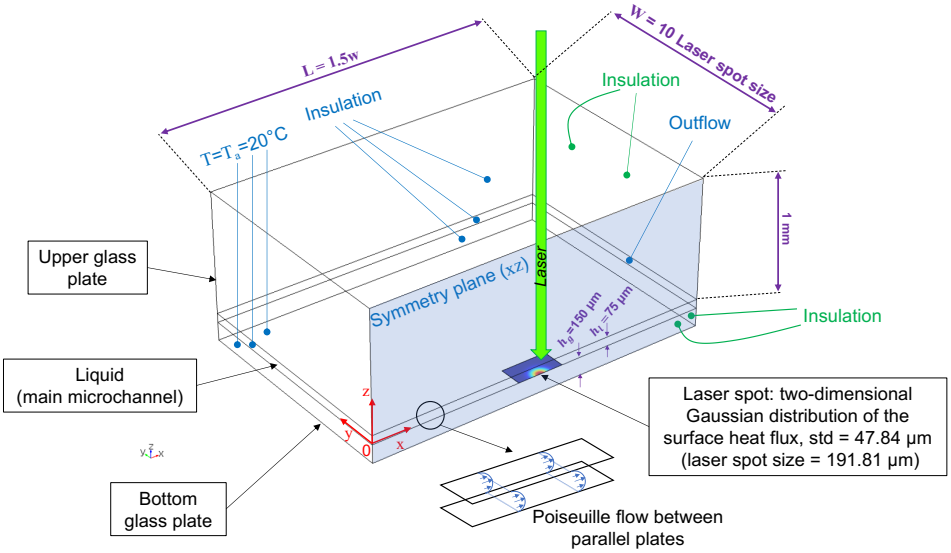

Fig. SM 1: The geometry considered for the numerical simulation of heat transfer in the SERS microfluidic chip and the associated boundary conditions.

Concerning the liquid flow, due to the very high aspect ratio of the main microchannel (6 mm $\times$ 75 μm), the flow corresponds to a Poiseuille flow between parallel plates and the velocity field $\boldsymbol{u}$ is given by the following parabolic relationship along the z-axis:

$$\boldsymbol{u}(z) = \frac{3}{2}\frac{Q}{S}\left(1 - \left(\frac{z - h_l/2}{h_l/2}\right)^2\right)\overrightarrow{e_x}, \tag{1}$$

where S and h_l are respectively the cross-section (6 mm $\times$ 75 μm) and the depth (75 μm) of the main microchannel and $\overrightarrow{e_x}$ the unit vector of the x-axis. A density of 1000 kg/m^3 and a heat capacity of 4180 J/kg/K was used for the liquid domain.

1.1 Boundary conditions

The heat production at the location of the laser spot (on the SERS substrate) is modeled by a two-dimensional Gaussian distribution of the surface heat flux (Fig. SM 1). This

heat is then released in both the flowing liquid (mainly) and the bottom glass plate (a little). This is modeled using the following local heat flux balance at the interface between the liquid domain and the bottom glass plate ($z = 0$):

$$XP.g(x,y) - \lambda_g \left.\frac{\partial T_g}{\partial z}\right|_{z=0} + \lambda_w \left.\frac{\partial T_w}{\partial z}\right|_{z=0} = 0, \tag{2}$$

where X is the absorption coefficient (ratio between the heat release and the laser power P), $g(x,y)$ a two-dimensional Gaussian distribution, λ_g and λ_w the thermal conductivities of glass and water respectively (λ_g = 1.2 W/m/K and λ_w = 0.6 W/m/K), T_g and T_w the temperature fields in the glass plate and in the liquid respectively. For the interface between the liquid domain and the upper glass plate ($z = h_l$), the continuity of the heat flux is applied, $\lambda_g dT_g/dz|_{z=h_l} = \lambda_w dT_w/dz|_{z=h_l}$. The continuity of the temperature is also applied using Dirichlet conditions on the temperature at each interface between the liquid domain and the two glass domains. The standard deviation of the laser beam (47.94 μm), determined experimentally, is used as the standard deviation of $g(x,y)$.

Concerning the boundary conditions of the lateral surfaces, parallel to the z-axis (constant ambient temperature, insulation and outflow, Fig. SM 1), they are placed sufficiently away from the laser spot to avoid interfering effects. The width W and length $L = 1.5W$ of the blocks were varied to find from which value of W the numerical result becomes independent of the block size; the value W = 10 $\times$ laser spot size (192 μm) was determined.

For the glass blocks, the boundary conditions of the horizontal surfaces exposed to air are insulating conditions. Natural convection, which could enhance heat transfer, should not act significantly here because of i) the large lateral size of the glass plates $\sim$5 cm (limiting the development of air flow by convection) and ii) the low local overheating

at the surface of the glass plates, < 2.5°C for the upper surface and < 5.5°C for the lower surface. The Rayleigh number is estimated to be lower than 70.10^3, assuming that all the surface is overheated (this is therefore an overestimation). From this value and the correlations providing the Nusselt number, for plates with upper or lower hot surface [1], low Nusselt numbers, close to the unity, are obtained. Such a value for a Nusselt number usually describes heat transfer by conduction only. Consequently, one can use the following boundary condition, heat flux density = $h(T - T_a)$, in which the exchange coefficient h is directly related to the constant value of the Nusselt number by $h = \lambda_a Nu/l$, where λ_a is the thermal conductivity of the air and l the length scale of the system (we select l = 5 cm here and λ_a = 0.025 W/m/K). Computations were performed by varying the value of h (from 0 to $h = \lambda_a Nu/L$). The target parameters, the steady state temperature at 1 mm behind the laser spot, $T^{SS}_{1\,\mathrm{mm}}$, and the steady state maximum temperature at the laser spot, T^{SS}_{ls}, were found to be almost not dependent on the value of h and this is why an insulating condition was selected.

1.2 Mesh

Concerning the mesh, a fine mesh was used in the region of the laser spot (mesh size = laser spot size / 60) and a progressively coarser mesh was applied in the rest of the volume (the maximum size is 150, 75 and 15 μm for the upper glass plate, liquid domain and lower glass plate respectively). A mesh convergence analysis was performed to determine the minimum mesh size to use in the laser spot region.

1.3 Determination of the light absorption coefficient X

The input heat power is adjusted in order to making match $\Delta T^{SS}_{1\,\mathrm{mm}}$ determined numerically to $\Delta T^{SS}_{1\,\mathrm{mm}}$ determined experimentally. This is shown for the case P = 50 mW in Fig. SM 2, where $\Delta T^{SS}_{1\,\mathrm{mm}}$ is plotted as a function of the flow rate Q. The value of the input heat power used in the simulation is varied until the simulation curve coincide with the experiment curve (a least mean squares process is used). An absorption coefficient of 46.0% is thus determined by dividing the input heat power by the laser power (50 mW). From this value of the absorption coefficient, ΔT^{SS}_{ls} is numerically determined for the values of both P and Q used in experiments (Fig. 5).

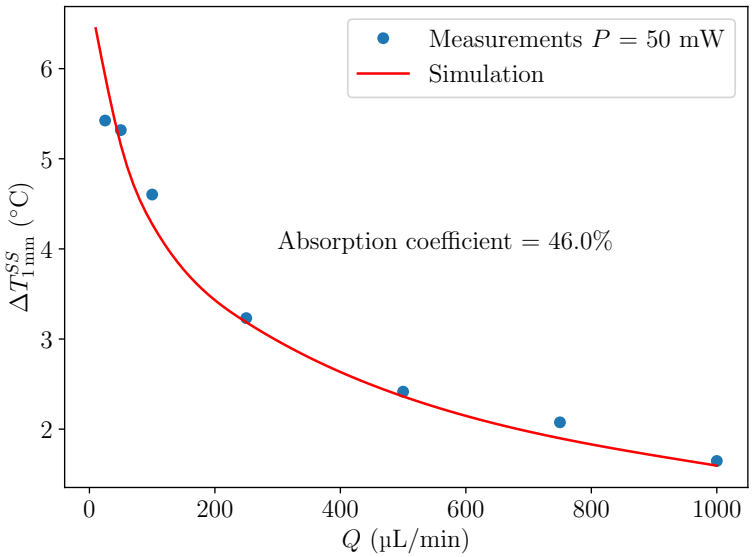

Fig. SM 2: $\Delta T^{SS}_{1\,\mathrm{mm}}$ as a function of Q, for P = 50 mW, from the measurements (blue disks) and from the simulation of heat transfer in the SERS microfluidic chip (red curves); matching the simulation curve with experiments allows determining the amount of laser power converted into heat, an absorption coefficient of 46.0% is thus determined.

1.4 Results

A typical result is shown in Fig. SM 3a, where iso-temperature surfaces are plotted in the liquid and the bottom glass plate domains, for a heat power XP of 5 mW and a liquid flow rate of 500 μL/min. The temperature profile along the bottom surface of the main microchannel ($z = 0$), passing through the laser spot ($y = 0$) and along the x-axis is shown in Fig. SM 3b (red solid line). The location of the center of the laser spot is indicated by the vertical black dashed line. The temperature at the laser spot T_{ls}^{SS} is numerically determined at this location (there is a slight shift with the maximum temperature because of the liquid flow). The temperature profile along the lower surface of the bottom glass plate ($z = -h_g$, h_g being the thickness of the bottom glass plate) is also shown in Fig. SM 3b (blue dashed line). Interestingly, due to heat dispersion by the flow, this temperature profile is rather flat in the zone probed by the micro-thermocouple (indicated by the grey stripe). $T_{1\,\mathrm{mm}}^{SS}$ is numerically determined by averaging the temperature in this region.

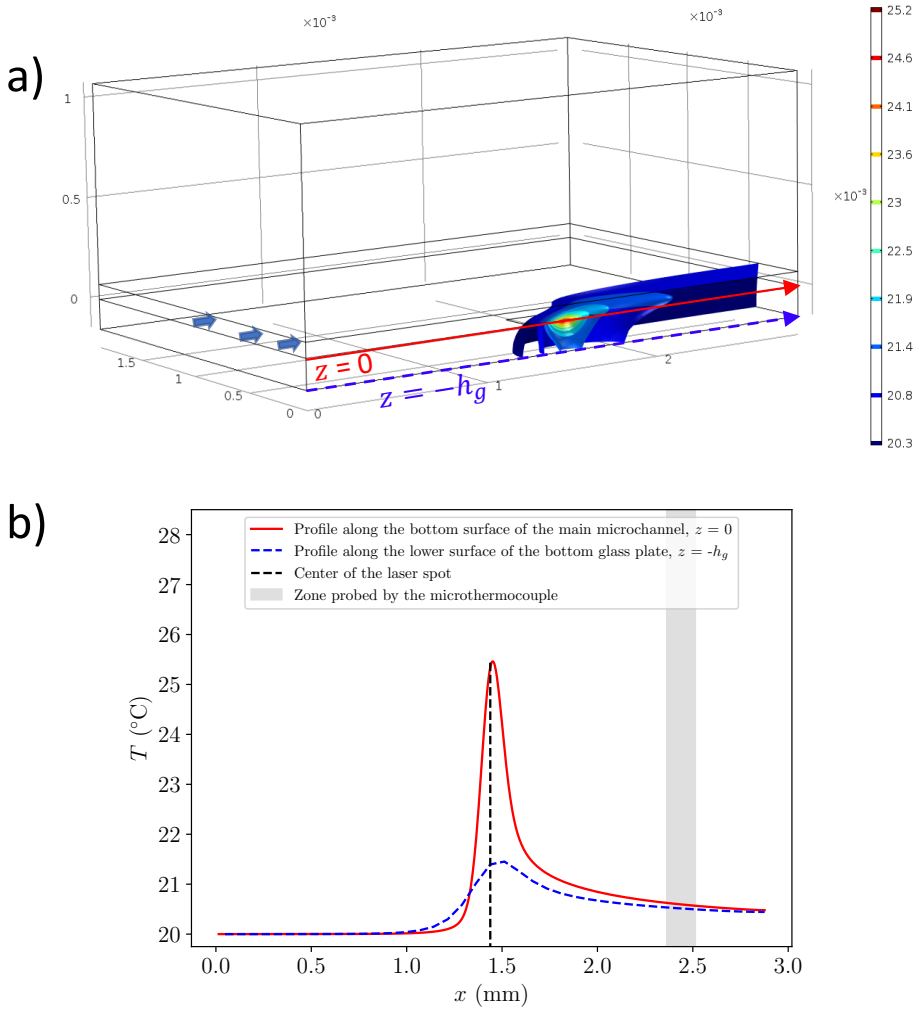

Fig. SM 3: a) Iso temperature surfaces in liquid and bottom glass domains obtained by 3D simulation of heat transfer in the SERS microfluidic chip. b) Temperature profiles along the x-axis for $y = 0$ along the bottom surface of the main microchannel ($z = 0$) and along the lower surface of the bottom glass plate ($z = -h_g$); the vertical black dashed line indicates the center of the laser spot and the grey stripe indicates the zone probed by the micro-thermocouple in the experiments (width of 150 μm). Results obtained for Q = 500 μL/min and XP = 5 mW.

2 Linear dependence of I_{SERS} with the concentration c and limit of detection

The intensity of the steady state SERS spectrum of CV is plotted as a function of CV concentration in Fig. SM 4. The limit of detection is estimated ∼5 nM, see the inset in Fig. SM 4.

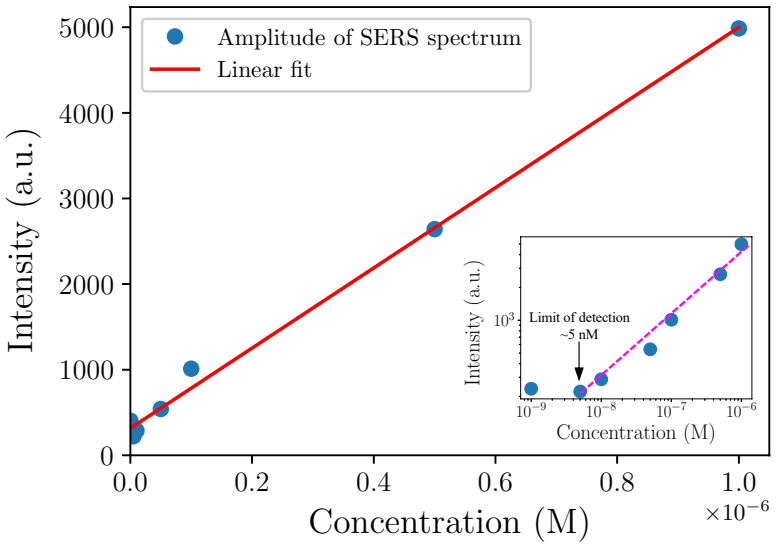

Fig. SM 4: Intensity of the steady state SERS spectrum of CV as a function of CV concentration, inset: log-log plot. Laser power P = 50 mW, liquid flow rate Q = 10 μL/min, IT = 0.1 s. Intensity measured by the intensity of the peak at 1180 cm^{-1}. SERS spectra acquired after 1 min of laser exposure.

3 Verification of the two-dimensionality of the concentration field

The steady state concentration field of CV in the main microchannel is obtained by numerical simulation using the software Comsol. The considered geometry is a rect-

angular block in which the solutions enter from the two half-faces and exit from the opposite face, as shown in Fig. SM 5.

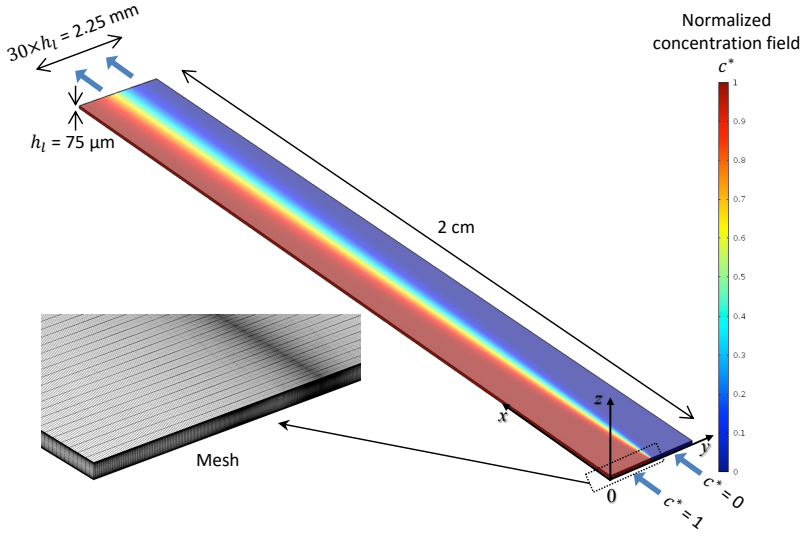

Fig. SM 5: The 3D fluid domain considered to solve the advection-diffusion problem in the main microchannel, the mesh used is also shown.

The length of the domain (2 cm) corresponds to the distance, from the inlet of the main microchannel (initial contact between the two streams) to the location where the concentration and SERS profiles are analyzed (Fig. 10, 11 and 12). The width of the domain is taken as 30× the microchannel depth h_l = 75 μm. The transport equation for CV is solved in this 3D domain:

$$\boldsymbol{u}.\boldsymbol{\nabla} c^* = D\left(\frac{\partial^2 c^*}{\partial x^2} + \frac{\partial^2 c^*}{\partial y^2} + \frac{\partial^2 c^*}{\partial z^2}\right), \tag{3}$$

where c^* is the dimensionless normalized concentration ($c^* = (c - c_{low})/(c_{high} - c_{low})$, with c_{low} and c_{high} the CV concentrations of the weakly and highly concentrated streams respectively) and $\boldsymbol{u}$ the velocity field of the Poiseuille flow given by Eq. SM 1.

3.1 Boundary conditions

Fixed concentration conditions are applied at the two inlet half-faces, $c^* = 1$ and $c^* = 0$ for the weakly and highly concentrated stream respectively (Fig. SM 5). An outflow boundary condition is applied at the outlet. For the remaining surfaces, no flux boundary conditions are applied.

3.2 Mesh

The domain is meshed using a fine mesh near the horizontal microchannel walls, $z = 0$ and $z = h_l$, as well as in the contact zone between the two streams, $y = 15h_l$, as shown in Fig. SM 5. Along the z-axis, the minimal mesh size is 0.4 μm which is lower than $1/65$ of the lowest value of the diffusion length at a distance of 2 cm, $\delta(2\text{cm})$, 26 μm (for the fastest flow Q = 1000 μL/min), and along the y-axis, the minimal mesh size is 2 μm which is lower than $1/13$ of the same value; a progressively coarser mesh was applied in the rest of the volume (the maximum mesh size is 3.4 and 9.5 μm along z-axis and y-axis respectively). A mesh convergence analysis was performed to validate the mesh configuration.

3.3 Results

The obtained concentration field at the outlet of the fluid domain (equivalent to the observation zone in experiments), $c^*(x = 2\,\text{cm}, y, z)$, is shown for several flow rates Q in the range covering the range used in experiments [2, 1000 μL/min] in Fig. SM 6. For $Q < 250$ μL/min, the concentration field is effectively two-dimensional. A progressive deviation to the two-dimensionality is visible for $Q \geq 250$ μL/min. The concentration profiles at the outlet of the domain (x = 2 cm), at the middle ($z = h_l/2$) and at the bottom

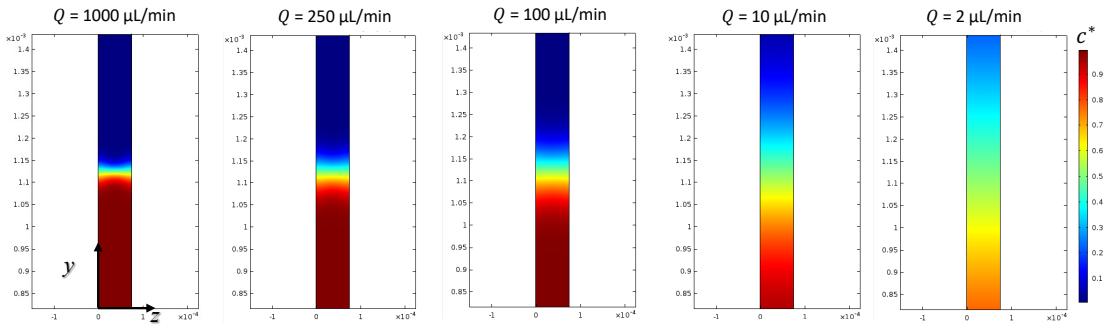

Fig. SM 6: Concentration field at the outlet of the fluid domain, $c^*(x = 2\,\mathrm{cm}, y, z)$, for several flow rates Q.

wall ($z = 0$) of the main microchannel, are shown in Fig. SM 7a. In addition, the theoretical prediction (Eq. 8), adapted to two-dimensional concentration fields, is also shown. For each flow rate, the three curves coincide rather well. However, a notable

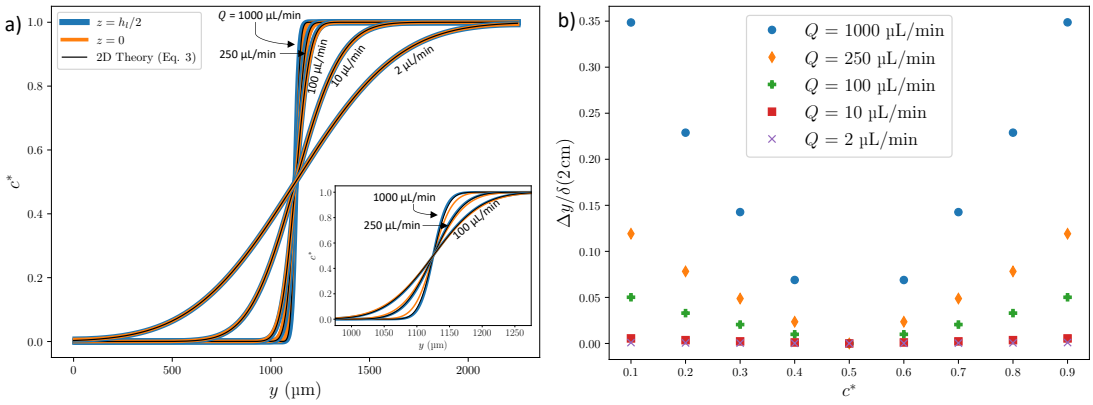

Fig. SM 7: a) Normalized concentration profiles from the simulation, $c^* = f(y)$, at a distance of 2 cm from the inlet of the two streams in the fluid domain of the main microchannel (x = 2 cm), and at the middle ($z = h_l/2$, blue solid lines) and at the bottom wall ($z = 0$, orange solid lines) of the main microchannel, and the theoretical normalized concentration profile adapted to two-dimensional concentration fields (Eq. 8, black solid lines), for several flow rates Q (indicated near the corresponding curves); the inlet is a magnified view of the concentration gradient for Q = 1000, 250 and 100 μL/min. b) Position shift Δy induced by the difference between the middle and bottom wall profiles, evaluated every tenth from 0 to 1, for all Q values investigated.

difference is visible for the higher flow rates 1000 and 250 μL/min as highlighted in the inset of Fig. SM 7a. This is due to an enhanced diffusion near the wall compared to the middle where the flow velocity is higher [2, 3].

To analyze in more detail the gap between the profile curves, the difference between the profiles, at the middle and at the bottom wall, can be quantified by the position shift Δy which is defined here as:

$$\Delta y(c^*) = \mathrm{abs}\left(y[c^*(z=0)] - y[c^*(z=h_l/2)]\right). \tag{4}$$

To estimate the degree of distortion of the concentration field, relatively to the diffusion length $\delta(2\mathrm{cm})$ ($\sim$size or width of the gradient), the ratio $\Delta y/\delta(2\mathrm{cm})$ is plotted as a function of c^*, for every tenth from 0 to 1, and for the various flow rate values in Fig. SM 7b. It is found that, for $Q \leq 250$ μL/min, $\Delta y/\delta(2\mathrm{cm})$ is lower than 12% which shows that the concentration field can effectively be considered as two-dimensional (see also the image of the concentration field at the outlet of the microchannel Fig. SM 6 for $Q \leq 250$ μL/min), and the theory applies (Eq. 8). For $Q = 1000$ μL/min, $\Delta y/\delta(2\mathrm{cm})$ reaches 35% which shows that the concentration field is significantly distorted (as it can be seen in the image of the concentration field for $Q = 1000$ μL/min in Fig. SM 6). Consequently, for Q = 1000 μL/min the concentration field cannot be considered as two-dimensional and therefore the 2D theory (Eq. 8) is not expected to apply.

References

[1] T. L. Bergman, T. L. Bergman, F. P. Incropera, D. P. Dewitt, and A. S. Lavine, *Fundamentals of heat and mass transfer*. John Wiley & Sons, Hoboken, USA,

2007.

[2] R. F. Ismagilov, A. D. Stroock, P. J. A. Kenis, G. Whitesides, and H. A. Stone, "Experimental and theoretical scaling laws for transverse diffusive broadening in two-phase laminar flows in microchannels," *Applied Physics Letters*, vol. 76, pp. 2376–2378, 04 2000.

[3] J.-B. Salmon and A. Ajdari, "Transverse transport of solutes between co-flowing pressure-driven streams for microfluidic studies of diffusion/reaction processes," *Journal of Applied Physics*, vol. 101, p. 074902, 04 2007.